نشریه ژئومکانیک و ژئوانرژی (ژئومکانیک نفت)

Geomechanics and Geoenergy Journal (GGJ)

Original article

Application of Extended Finite Element Method for Simulating Crack Initiation and Propagation Mechanism in Hydraulic Fracturing Process

Mohammad Reza Zeerak[1], Mohammad Fatehi Marji[2*], Manouchehr Sanei[3], Mehdi Najafi[4], Abolfazl Abdollahipour[5]

1- PhD Student in Rock Mechanics, Faculty of Mining and Metallurgy, Yazd University, Yazd, Iran
2- Professor, Engineering Department, Faculty of Mining and Metallurgy, Yazd University, Yazd, Iran
3- Assistant Professor, Engineering Department, Faculty of Mining and Metallurgy, Yazd University, Yazd, Iran
4- Professor, Engineering Department, Faculty of Mining and Metallurgy, Yazd University, Yazd, Iran
5- Assistant Professor, School of Mining Engineering, College of Engineering, University of Tehran, Tehran, Iran

Received: 2025/8/28; Accepted: 2025/12/25

DOI: 10.22107/ggj.2025.509057.1250

Keywords

Extended Finite Element Method (XFEM)
B-K Fracture Criterion
Crack Initiation
Hydraulic Fracturing
Crack Propagation

Abstract

The Extended Finite Element Method (XFEM) is a powerful numerical method for simulating crack initiation and propagation, particularly in unconventional hydrocarbon reservoirs such as shale and tight gas formations. This study utilizes XFEM to investigate the evolution of hydraulic fractures, specifically focusing on the influence of crack geometry, including crack length and initial orientation, on fracture behaviour. Unlike previous works that have primarily aimed to validate the general applicability of XFEM in hydraulic fracturing simulations, the present research centers on understanding how variations in crack geometry affect stress intensity factors (SIFs), displacement fields, and fracture propagation paths. Rather than emphasizing XFEM's well-known numerical strengths, this study highlights its capacity to capture complex fracture-rock interactions within low-permeability and geologically heterogeneous formations. The XFEM framework enables a detailed examination of fluid-driven crack growth under varying mechanical and geometrical conditions. Results demonstrate that increasing crack length leads to higher SIFs and displacement magnitudes, promoting faster fracture propagation. Furthermore, the initial crack angle significantly alters propagation trajectories, with cracks showing a tendency to reorient toward directions of maximum stress concentration. These findings reveal key insights into fracture mechanics in unconventional settings and underscore the complex interplay between crack geometry, stress distribution, and hydraulic forces. Overall, the study confirms XFEM's potential as a reliable and accurate modeling tool for optimizing hydraulic fracturing design and enhancing recovery efficiency in unconventional reservoirs. It is recommended that future studies incorporate thermal effects into fracture behavior analyses, as temperature variations can have a significant impact on stress fields, material properties, and crack propagation under deep subsurface conditions.

1. Introduction

Hydraulic fracturing (HF) is a well-established technique for stimulating hydrocarbon-bearing formations by enhancing their permeability, thereby facilitating the efficient flow of hydrocarbons toward the wellbore [1]. Due to its high success rate and favorable economic returns, this technique is widely employed in unconventional reservoirs. Wells that experience production decline after the initial hydraulic fracturing treatment and become economically unfeasible can undergo refracturing to restore productivity and extend their operational lifespan. The development of shale gas and shale oil reservoirs has significantly transformed the global energy market, driving rapid growth in exploration and production (E&P) activities. However, the extremely low permeability and

* **Corresponding Author:** mfatehi@yazd.ac.ir / mohammad.fatehi@gmail.com.

porosity of these reservoirs necessitate hydraulic fracturing for their economic viability. The process involves injecting high-pressure fluid into the formation, inducing fractures that create preferential flow paths for hydrocarbons. In formations with pre-existing natural fractures, the interaction between hydraulic fractures and these fractures significantly influences the fracture propagation pattern, whereas in formations lacking natural fractures, hydraulic fractures primarily propagate in the direction of the maximum principal stress [2]. Traditionally, hydraulic fracturing design has relied primarily on empirical methods. However, given the high costs associated with drilling, fluid injection, and proppants, there is an increasing need for physics-based numerical modeling to accurately predict fracture behaviorand optimize operational parameters. Numerical simulations enable the prediction of key fracture characteristics such as length, width, and efficiency, thereby improving the cost-effectiveness and operational success of hydraulic fracturing treatments (Fig. 1).

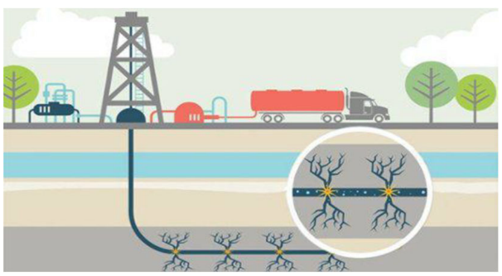

Fig. 1. Hydraulic fracturing treatment [3].

Hydraulic fracturing has been utilized since the early days of the petroleum industry. The first experimental operation was conducted in 1947 on a gas well operated by Stanolind Oil in the Hugoton field, located in Grant County, Kansas, USA. The benefits of hydraulic fracturing extend beyond enhancing well productivity. It has also contributed to increasing hydrocarbon reserves through improving recovery from existing reservoirs, enabling the economic development of unconventional resources, and facilitating the commercial development of previously uneconomic hydrocarbon reservoirs. For example, in the United States, the widespread application of hydraulic fracturing has been associated with significant increases in estimated oil and natural gas reserves, with reported increases of approximately 30% and 90%, respectively [4]. In 1949, HOWCO (Halliburton Oil Well Cementing Company), the exclusive patent holder, carried out a total of 332 well stimulation operations, achieving an average production increase of 75%. It is estimated that approximately 2.5 million hydraulic fracturing operations have been performed globally, with around 60% of the wells drilled today undergoing fracturing [5]. Zuorong Chen (2013) in the study titled "An ABAQUS Implementation of the XFEM for Hydraulic Fracture Problems", developed a finite element framework integrating XFEM for simulating hydraulic fractures without remeshing. The approach incorporates fluid pressure degrees of freedom to model fluid flow within cracks and its effect on deformation, ensuring coupled solutions for fluid flow and crack propagation. The study highlights XFEM's efficiency and precision in solving complex hydraulic fracture problems, demonstrating its potential for such simulations [6].

Moradi et al. (2016) studied the interaction between hydraulic fractures and natural fractures in fractured hydrocarbon reservoirs using the indirect boundary element method. The study analyzed hydraulic fracture behaviorunder various conditions in interaction with natural fractures, validating the numerical method with analytical solutions. The results showed that hydraulic fractures tend to pass through natural fractures, but the likelihood of passage decreases after each interaction [7]. Abdollahipour et al. (2016) studied the impact of crack geometry parameters on hydraulic fracturing processes in hydrocarbon reservoirs. They modeled various geometric parameters of initial hydraulic fractures, including patterns, distances, crack length, and wellbore fracturing phase angles, using a higher-order displacement discontinuity method in horizontal and vertical wells. The study observed well-known hydraulic fracturing issues such as crack interference and termination in specific patterns, and identified the optimal arrangement for better fracture production. The results confirmed existing field measurements and determined the optimal fracturing phase angle for vertical wells [8].

Cruz et al. (2019) developed an XFEM implementation in ABAQUS to simulate hydraulic fracturing in porous rocks, focusing on fracture intersections. The tool couples hydro-mechanical behaviorand allows fluid exchange between fractures and the porous medium. It overcomes ABAQUS' limitation of handling multiple fractures in one element [9]. Dontsov and R. Suarez-Rivera (2020) studied the simultaneous propagation of multiple hydraulic fractures in homogeneous rocks under limited entry conditions. They found that in viscosity-dominated regimes, fractures grow symmetrically with minimal interaction, while in toughness-dominated regimes, fractures interact strongly, forming segmented, petal-like geometries. The research examined factors such as fluid types, stress anisotropy, and fracture toughness anisotropy. It was found that fracture spacing significantly affects interactions, with smaller spacings leading to stronger interactions, especially in toughness-dominated regimes. [10].

Azarov et al. (2021) studied hydraulic fracture propagation near a circular cavity in poroelastic media using XFEM in ABAQUS. The results showed that the fracture path is highly influenced by hydrostatic stress and the distance between the initial crack and cavity, with shorter distances and higher stresses leading to greater curvature [11]. Heydari et al. (2022) studied the effects of in-situ stresses and porosity on hydraulic fracture growth. They found that fractures propagate parallel to the maximum principal stress and deviate in the least resistant direction. Increased in-situ stress difference reduces fracture pressure. Shear stresses cause fracture rotation when the initial crack is not aligned with the principal stresses. Lower fracture pressure is required for cracks at angles less than 45° to the maximum stress, and increasing porosity reduces the material's stiffness while potentially increasing crack opening [12].

Zeerak et al. (2023) conducted a study titled "Investigating Hydraulic Fracture Models for Production Enhancement from Unconventional Hydrocarbon Reservoirs". The study reviewed numerical modeling approaches and compared their applications in hydraulic fracturing simulations, offering a comparative analysis of various methods along with their respective advantages and limitations. This review enhances the understanding of numerical techniques applied in hydraulic fracturing and provides valuable guidance for future research focused on boosting production from unconventional reservoirs [13]. Fatehi Marji et al. (2023), in their study titled "The Explosive Fracturing Technique Analysis for Highly Low Permeable Reservoirs Using Analytical, Displacement Discontinuity, and Finite Difference Coupled Method", investigated the simulation of crack initiation and propagation in reservoir rocks using an explosive fracturing technique. Their findings indicate that this method can effectively improve both permeability and production in highly low-permeable reservoirs, particularly in horizontal wells [14]. Esfandiari and Pak (2023) examined the impact of in-situ stresses on hydraulic fracture characteristics using XFEM modeling and compared it with classical KGD and PKN models. They discovered that the simplifying assumptions of KGD and PKN models fail to capture the effects of in-situ stresses on fracture length, width, and fluid pressure. They proposed correction factors to enhance the accuracy of the KGD and PKN models, especially for reservoirs with critical in-situ stress conditions, stressing the importance of incorporating in-situ stresses in hydraulic fracturing design [15].

Zeerak et al. (2025) investigated crack growth mechanisms in hydraulic fracturing using the Extended Finite Element Method and a BEM-based verification approach. Their study focused on the effects of crack orientation and material properties on fracture behaviour. The results showed that lower-angle cracks propagated more easily, while higher angles led to complex mixed-mode propagation. A 120° crack orientation provided the greatest improvement in permeability and fracture stability. Furthermore, reductions in elastic or shear modulus increased crack aperture due to decreased stiffness, whereas Poisson's ratio had only a minor stiffening effect. These findings contribute to enhancing numerical prediction and optimization of hydraulic fracturing designs [16]. Yazdani et al. (2025), investigated the impact of hydraulic fracturing on sand production in low-strength reservoirs. The research explores how hydraulic fracturing affects sand production by using a two-dimensional model created with the discrete element method in PFC2D software. The results show a variation in sand production rates compared with the intact formation, highlighting the importance of understanding the interaction between hydraulic fracturing and sand production to optimize reservoir recovery and maintain well integrity [17].

The literature review encompasses a broad range of previous studies addressing different aspects of hydraulic fracturing, including fracture propagation, fluid pressure effects, fracture behavior in porous media, in-situ stress conditions, and initial crack geometry. Although these studies have significantly contributed to understanding hydraulic fracture mechanisms, many existing studies employ generalized approaches and provide limited systematic evaluation of the individual effects and interactions of fracture-related parameters within the XFEM framework. In contrast, the present study focuses on the fundamental mechanical aspects of crack initiation and propagation associated with hydraulic fracturing using XFEM. A series of parametric analyses are performed to investigate the effects of crack length on displacement components (U1 and U2), crack orientation on stress distribution (S11 and S22), crack geometry on propagation patterns, fracture toughness (KIc), and numerical parameters including mesh size, element type, and boundary conditions. The main contribution of this study is the establishment of a systematic XFEM-based framework for evaluating the influence of fracture-related parameters on crack evolution behavior, providing quantitative insights into the mechanisms governing fracture initiation and propagation. This systematic investigation provides deeper insight into the mechanical behavior of fracture evolution within the XFEM framework.

It should be noted that the present model primarily focuses on the fracture mechanics aspects of hydraulic fracturing and does not consider the effects of fluid flow, pore pressure evolution, fluid leak-off, or thermal variations. Accordingly, the proposed framework is intended to clarify the fundamental mechanical mechanisms of fracture initiation and propagation, while acknowledging that fully coupled processes are required for more realistic hydraulic fracturing simulations. These coupled processes represent important factors in practical hydraulic fracturing applications and will be incorporated in future studies to further improve the applicability of the proposed approach.

Table 1. Summary of Previous Studies on Hydraulic Fracturing Modeling Approaches.

Number	Authors	Year	Methodology	Principal findings
1	Zuorong Chen	(2013)	XFEM	XFEM enabled accurate simulation of fluid–crack interaction without remeshing in ABAQUS.
2	Moradi et al.	(2016)	IBEM	Hydraulic fractures often cross natural fractures, but passage likelihood declines with repeated interactions.
3	Abdollahipour et al.	(2016)	HODDM	Fracture geometry affects growth; optimal spacing and phase angles improve stimulation efficiency.
4	Cruz et al.	(2019)	XFEM	XFEM-ABAQUS implementation allowed coupled fluid exchange and multi-fracture modeling within porous media.
5	Dontsov and R. Suarez-Rivera	(2020)	BEM / DDM	Fracture interaction depends on regime; smaller spacing increases interaction under toughness dominance.
6	Azarov et al.	(2021)	XFEM	Fracture path curvature is governed by hydrostatic stress and initial crack distance from cavities.
7	Heydari et al.	(2022)	DDM	Fracture growth direction and pressure are influenced by in-situ stress orientation and rock porosity.
8	Zeerak et al.	(2023)	Review paper	Compared modeling methods for hydraulic fracturing; identified their strengths and applications in production.
9	Fatehi Marji et al.	(2023)	DDA	Explosive fracturing improved permeability in low-permeability formations, especially in horizontal wells.
10	Esfandiari and Pak	(2023)	XFEM, KGD	XFEM captured in-situ stress effects better than classical models; correction factors were proposed.
11	Zeerak et al.	(2025)	XFEM & BEM	120° cracks showed better propagation and permeability; stiffness reduction increased aperture.
12	Yazdani et al.	(2025)	DEM	Hydraulic fracturing changed sand production patterns; DEM modeling aids recovery and well integrity.

2. Linear Elastic Fracture Mechanics

Materials with low fracture resistance may fail at stresses significantly lower than their nominal strength and can be analyzed using LEFM, applicable to high-strength materials like those in aerospace, steels, rocks, ceramics, and concrete. EPFM, used for materials with plastic deformation, builds on LEFM concepts. Crack analysis in LEFM focuses on stresses at the crack tip and the stress intensity factor (K), assuming Hooke's law applies and the dissipative zone is negligible.

Residual strength refers to a material property similar to tensile or yield strength, rather than a stress value. Fracture occurs when the applied stress reaches the residual strength, σ_{res}. Fig. 2 illustrates the relationship between σ_{res} and crack size (a). For a maximum permissible crack length a_p, there is a corresponding maximum allowable stress σ_p that can be applied to the structure, which is significantly lower than the yield strength, σ_{yield}. As the crack size increases, the residual strength of the structure decreases progressively, as depicted in Fig. 2 [18].

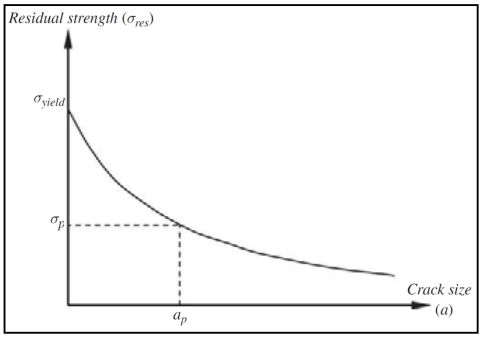

Fig. 2. Residual strength curve [18].

LEFM offers several advantages over conventional strength-based approaches by incorporating dissipative energy processes, such as plastic flow and microcracking, into a simple framework. This is especially useful when the dissipation zone is much smaller than the length of the fracture, as seen in the plateau region for (K_{Ic}) in Fig. 3 [19].

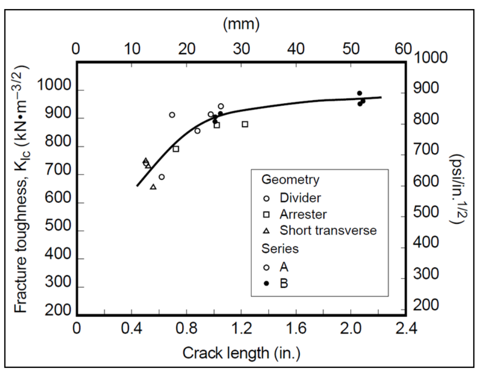

Fig. 3. Scale dependence of fracture toughness [19].

Irwin (1957) categorized singular stress fields around a crack tip into Mode I (opening), Mode II (shearing), and Mode III (tearing). In hydraulic fracturing, Mode I is key, while other modes appear in complex cases like fracture deflection. He also simplified the calculation of the stress intensity factor (K_I) for 2D cracks under constant pressure.

$$K_I = \sqrt{\pi L} p_{net} \tag{1}$$

Where L is the crack length and p_{net} is the net internal pressure opening of the crack. For a radial crack, the stress intensity factor can be expressed as:

$$K_I = 2\sqrt{\frac{R}{\pi}} p_{net} \tag{2}$$

Here R is the crack radius. Fracture toughness K_{Ic} is a widely recognized property linked to the specific fracture surface energy (γ_F).

$$K_{Ic} = \sqrt{\frac{2E\gamma_F}{1-v^2}} \tag{3}$$

This energy accounts for localized dissipative mechanisms occurring during fracture propagation and can be experimentally measured in laboratory settings [19].

2.1. Evaluation of the Fracture Toughness

To demonstrate the measurement of fracture toughness and the effect of a crack on material behaviour, we consider a bar of unit thickness featuring a central crack of length (2L) as shown in Fig. 4. While this configuration represents a simplified geometry, conducting such a tensile fracture test in practice presents significant challenges. It is assumed that the crack length is much smaller than the bar's width, and the width is significantly smaller than the bar's length. The stress intensity factor for this specific geometry is expressed as follows:

$$K_I \approx \sigma \sqrt{\pi L}\left(1 - \frac{L}{2b}\right)\left(1 - \frac{L}{b}\right)^{-1/2} \tag{4}$$

The applied stress (σ) defined as $F/2b$, influences the load-displacement behaviorof the sample, as shown in Fig. 4. The load initially increases until crack propagation begins, after which it decreases during stable crack growth. If unloading occurs at this stage, the displacement is fully recovered, displaying behaviorcharacteristic of perfect brittleness rather than elasto-plasticity. The slope change in the load-displacement curve arises from the increased crack length, not from material properties, allowing the crack length to be estimated. The CSIF (K_{Ic}), is reached when crack propagation initiates.

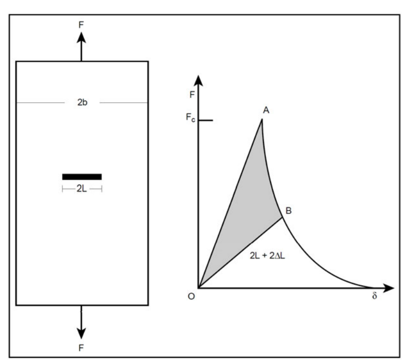

Fig. 4. Fracture toughness measurement: The shaded area on the left side of the plot indicates the energy required to propagate the crack from (2L) to ($2L + 2\Delta L$) [19].

$$K_{Ic} \approx \frac{F_c}{2b}\sqrt{\pi L}\left(1-\frac{L}{2b}\right)\left(1-\frac{L}{b}\right)^{-1/2} \quad (5)$$

where F_c is the critical load. As shown in Fig. 4, the area (OAB) represents the energy (dW_s) dissipated to propagate the crack from (2L) to ($2\Delta L$). The strain energy release rate is thus calculated as the dissipated energy divided by the newly created surface area, ($2\Delta L$).

$$G_e = \frac{dW_s}{2\Delta L} \quad (6)$$

A similar procedure can be applied when the crack propagates to the specimen boundary, resulting in.

$$G_e = \frac{dW_s}{2b} \quad (7)$$

In this case (dW_s) corresponds to the area under the load-displacement curve, with the initial crack length assumed to be negligible compared to the sample width ($\Delta L \cong b$). This approach eliminates the need to measure the crack length directly. For linear elastic behaviour:

$$G_e = \frac{1-v^2}{E}K_I^2 \quad (8)$$

Equation (8) defines the conditions under which the parameters (G_{Ic}) and (K_{Ic}^2) can be used in place of (G_e) and (K_I^2), respectively. The load-displacement curve presented in Fig. 4 can also be utilized to analyze the behaviorof the process zone [19].

3. Fracture propagation criterion

Two widely used approaches are available for modeling fracture propagation. The virtual crack closure technique Crack initiates when strain energy release rate exceed the critical (VCCT) relies on linear elastic fracture mechanics, predicting fracture growth when the energy release rate equals or surpasses a critical threshold. Conversely, the cohesive zone method (CZM) is based on Damage Mechanics, with fractures initiating when the damage criterion reaches its peak. In ABAQUS, moving fractures are modeled using both the cohesive segment method and the VCCT in conjunction with the enriched node technique. The key differences between the two criteria are outlined in Table 2.

Table 2. Differences between VCCT method and CZM - adapted from [20].

VCCT	CZM
Is contact (surface based)	Interface elements (element based) or contact (surface based)
Assumes an existing singularity	Can model fracture initiation
Brittle fracture using LEFM	Ductile fracturing occurring over a crack front modeled with cohesive elements
Requires G_I, G_{II} and G_{III}.	Requires E, σ_T and G_I, G_{II} and G_{III}
Crack initiates when the strain energy release rate exceeds the critical value.	Crack initiates when traction exceeds critical value
Crack surface are rigidly bonded when uncracked	Crack surfaces are joined elastically when uncracked

When using the VCCT criteria this is only verified for the fracture contact surface. In contrast, the cohesive zone method is applied to the entire analysis domain, which ensures that fracture initiation and propagation can occur at any point within the analysis domain [21].

3.1. SIF of Mixed Mode I-II Crack

The stress components of the mixed-mode I-II at the crack tip, expressed in polar coordinates, can be determined using the linear elastic method.

$$\sigma_r = \frac{1}{2\sqrt{2\pi r}}\left[K_I\cos\frac{\theta}{2}(3-\cos\theta)+K_{II}\sin\frac{\theta}{2}(3\cos\theta-1)\right] \quad (9)$$

$$\sigma_\theta = \frac{1}{2\sqrt{2\pi r}}\cos\frac{\theta}{2}\left[K_I(1+\cos\theta)-3K_{II}\sin\theta\right] \quad (10)$$

$$\sigma_{r\theta} = \frac{1}{2\sqrt{2\pi r}}\cos\frac{\theta}{2}\left[K_I\sin\theta+K_{II}(3\cos\theta-1)\right] \quad (11)$$

where K_I is the mode-I SIF, K_{II} is the mode-II SIF, r is the distance from the crack tip, and θ is the angle by which the crack surface deviates from the original crack-tip direction. Fig. 5 illustrates an infinite plate with a central crack of length ($2a$) subjected to biaxial loading ($\sigma_y^\infty, \sigma_x^\infty$ *and* $\sigma_x^\infty = k\sigma_y^\infty$).

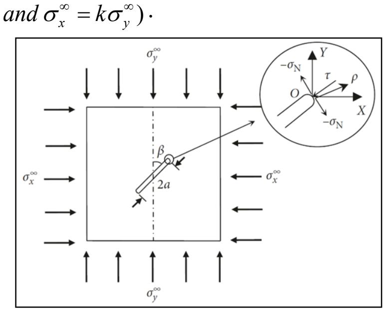

Fig. 5. External and internal stresses associated with a mixed-mode I-II crack in an infinite plate [22].

The stress state along the crack plane can be described as follows:

$$\sigma_T = \sigma_y^\infty \cos^2\beta + \sigma_x^\infty \sin^2\beta \tag{12}$$

$$\sigma_N = \sigma_y^\infty \sin^2\beta + \sigma_x^\infty \cos^2\beta \tag{13}$$

$$\tau = \left(\sigma_y^\infty - \sigma_x^\infty\right)\sin\beta\cos\beta \tag{14}$$

Where (σ_T), (σ_N), and (τ) represent the tangential, normal, and shear stresses respectively. Tensile stresses are considered positive, whereas compressive stresses are considered negative.

The stress intensity factor (SIF) varies depending on crack geometry and the presence of friction along the crack surfaces. (K_{IT}) and (K_{IN}) represent the SIF caused by transverse compressive stress and normal stress, respectively [22].

3.2. B-K Fracture Criterion

The original Benzeggagh–Kenane (B–K) fracture criterion is a widely adopted mixed-mode fracture criterion used for delamination analysis. It is derived based on the assumption of a common mixed-mode resistance to delamination [23]. Interlaminar damage is one of the most critical failure mechanisms in laminated materials, as it can significantly reduce a material's stiffness and strength. As a result, it represents a key failure mechanism that must be carefully evaluated when assessing the durability and damage tolerance of laminated material structures. This type of damage typically arises from Mode I, Mode II, or mixed-mode (Mode I+II) loading conditions. Crack propagation under pure Mode I (opening mode) and pure Mode II (shearing mode) cyclic loading has been widely studied in the literature. However, mixed-mode (Mode I + II) loading has attracted increasing attention because it more accurately represents practical loading conditions, as it more accurately reflects real-world conditions. In practice, material structures are typically subjected to a combination of Mode I and Mode II loading. Various test configurations have been proposed for mixed-mode loading, though many have practical limitations. Among the available techniques, the Mixed-Mode Bending (MMB) test introduced by Crews and Reeder is widely recognized because of its versatility. Aboura et al. further refined it for specific materials based on Reeder's work. The MMB test offers advantages such as enabling a wide range of mixed-mode ratios with a single specimen geometry, and the G_{II}/G_T ratio remains unaffected by crack length [24].

Crack propagation in a single-crack rock was simulated using commercial finite element software, employing the extended FEM and a cohesive model, without considering progressive damage evolution. The Benzeggagh–Kenane (B-K) model is expressed as follows [22]:

$$G_{TC} = G_{IC} + (G_{IIC} - G_{IC})\left(\frac{G_{II}}{G_T}\right)^m \tag{15}$$

where m is a characteristic parameter of the material considered. The delamination crack growth rate (da/dN) can be expressed as a function of the strain energy release rate (ΔG) through a relationship of the following form:

$$\frac{da}{dN} = B(\Delta G)^d \tag{16}$$

For each mode ratio (G_{II}/G_T), corresponding values of (d) and (B) are determined [24].

4. Governing Equations and Solution Procedures

This section briefly reviews the governing equations of elastostatics and presents their corresponding weak formulations. In particular, it addresses the scenario where an internal line exists, across which the displacement field may exhibit discontinuity. In fracture mechanics, the momentum equation governs the mechanical equilibrium and dynamic response associated with crack propagation. The equation can be written as:

$$\rho\frac{\partial \mathbf{v}}{\partial t} + \nabla\cdot\sigma + \mathbf{f} = 0 \tag{17}$$

Where ρ is the density of the material, $\mathbf{v}$ is the velocity field, σ is the stress tensor, $\mathbf{f}$ is the body force vector (e.g., gravitational forces), and $\nabla\cdot\sigma$ is the divergence of the stress tensor, representing internal forces within the material. Consider a domain Ω bounded by the surface Γ. The boundary Γ is divided into subsets Γ_u, Γ_t, and Γ_c, such that $\Gamma = \Gamma_u \cup \Gamma_t \cup \Gamma_c$, as illustrated in Fig. 6. Prescribed displacements are applied on Γ_u, while tractions are specified on Γ_t. The crack surfaces Γ_c are assumed to be traction-free, with cracks represented as lines in two-dimensional analyses and surfaces in three-dimensional analyses [25].

The equilibrium equations can be written as:

$$\nabla\cdot\sigma + F_b = 0 \qquad in\ \Omega \tag{18}$$

The boundary conditions can be expressed as:

$$\begin{aligned} \sigma \cdot \mathbf{n} &= F_{\bar{t}} && \text{on } \Gamma_t \\ \sigma \cdot \mathbf{n} &= 0 && \text{on } \Gamma_{c^+} \\ \sigma \cdot \mathbf{n} &= 0 && \text{on } \Gamma_{c^-} \end{aligned} \tag{19}$$

Where Γ_t is traction boundary, Γ_u is displacement boundary, Γ_c is crack boundary, σ is Cauchy stress tensor, F_b is body force vector, **n** denotes the unit outward normal vector, and F_t is external traction vector.

$$\varepsilon = \varepsilon(\mathbf{u}) = \nabla_s \mathbf{u} \tag{20}$$

Here ∇_S denotes the symmetric part of the gradient operator.

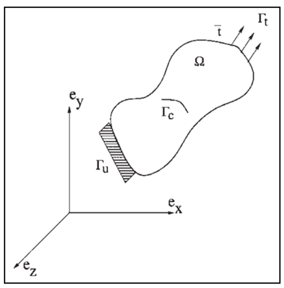

Fig. 6. Body with the internal boundary subjected to the loads [25].

The boundary conditions are as follows:

$$\mathbf{u} = \bar{\mathbf{u}} \quad \text{on } \Gamma_u \tag{21}$$

The constitutive relationship is governed by Hooke's law, which relates stress and strain in linear elasticity.

$$\boldsymbol{\sigma} = \boldsymbol{C} : \varepsilon \tag{22}$$

$\boldsymbol{\sigma}$ is the Cauchy stress tensor, ε is the strain tensor, and $\boldsymbol{C}$ is the Hooke's constant (stiffness tensor) which represents the material's elastic properties. The symbol (:) denotes the double-dot product of tensors.

In hydraulic fracturing analyses, fluid flow within fractures is described through the momentum conservation equation. This is typically done using the Navier-Stokes equation modified to account for fracture-induced flow:

$$\rho_f \left(\frac{\partial \mathbf{v_f}}{\partial t} + \mathbf{v_f} \cdot \nabla \mathbf{v_f} \right) = -\nabla p + \mu_f \nabla^2 \mathbf{v_f} + \mathbf{f} \tag{23}$$

Where ρ_f is the fluid density, $\mathbf{v_f}$ is the velocity field of the fluid, p is the pressure in the fracture, μ_f is the viscosity of the fluid, $\mathbf{f}$ is external forces such as gravity or fracture-induced forces.

This equation characterizes fluid transport within fractures under the influence of pressure gradients and viscous effects in the context of hydraulic fracturing. The fluid flow within the crack is described using lubrication theory, which is governed by Poiseuille's law.

$$q = -\frac{w^3}{12\mu} \frac{\partial p}{\partial x} \tag{24}$$

In this context, μ is the dynamic viscosity of the fracturing fluid. The flow rate (q), inside the crack per unit length along the x-direction is determined as the product of the average fluid velocity, $\bar{v}$, and the crack opening, w (Fig. 7) [26].

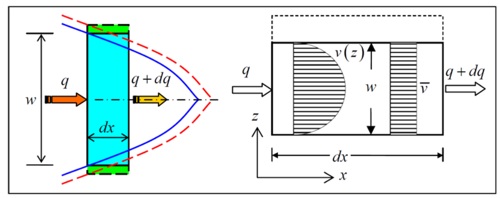

Fig. 7. Fluid flow within the crack [26].

$$q(x) = \bar{v}(x) w(x) \tag{25}$$

The fracturing fluid is assumed to be incompressible; therefore, the mass conservation equation can be written as follows:

$$\frac{\partial w}{\partial t} + \frac{\partial q}{\partial x} + g = 0 \tag{26}$$

The flux discontinuity (g) is defined as positive when fluid exits the fracture. It represents the fluid exchange rate between the fracture and the surrounding porous medium, such as porous rock. Substituting Equation (24) into Equation (26) yields the governing equation that describes the fluid flow within the fracture.

$$\frac{\partial w}{\partial t} - \frac{\partial}{\partial x}\left(k \frac{\partial p}{\partial x} \right) + g = 0 \tag{27}$$

Where $k = \dot{w}^3 / 12\mu$ is the permeability, the general form of the governing equation (27) can be written as:

$$\dot{w} - \nabla^T (\mathbf{k} \nabla p) + g = 0 \tag{28}$$

Here $\mathbf{k}$ is the permeability tensor. According to Linear Elastic Fracture Mechanics (LEFM), fracture propagation under quasi-static conditions occurs when the stress intensity factor reaches the critical fracture toughness of the material.

$$K_I = K_{Ic} \tag{29}$$

Where K_I is the Mode I stress intensity factor, representing the stress state near the crack tip under opening mode loading, and K_{Ic} is the material's fracture toughness, which defines the critical stress intensity required for fracture propagation. At the inlet boundary, the prescribed fluid flux is equal to the injection rate:

$$q\big|_{inlet}=Q_0 \tag{30}$$

Where q is the volumetric flow rate or mass flux at the specified location. $\big|_{inlet}$ Indicates the value of q at the inlet boundary of the system. Q_0 is a specified flow rate at the inlet, applied as a boundary condition.

At the fracture tip, the boundary conditions consist of zero fracture opening and zero fluid flux.

$$w\big|_{tip}=q\big|_{tip}=0 \tag{31}$$

The equations outlined above form a comprehensive framework for predicting the evolution of hydraulic fractures [26].

5. Numerical Solutions

5.1. Finite Element Method

The finite element method (FEM) is one of the most widely used numerical methods for solving complex engineering problems by dividing a complex system into smaller, manageable components called finite elements through spatial discretization, achieved via meshing. This process transforms boundary value problems into systems of algebraic equations, approximating the unknown function over the domain. These individual element equations are then assembled into a larger system representing the entire problem, with the numerical solution obtained through the assembly and solution of the resulting algebraic system [27]. The weak form of the equations for the finite element method can be expressed as the following, where the set of allowable displacement fields is characterized by:

$$\mathcal{U}=\{\mathbf{v}\in\mathcal{V}:\mathbf{v}=\bar{\mathbf{u}}\ \text{ on }\Gamma_u\mathbf{v}\text{ discontinuous on }\Gamma_c\} \tag{32}$$

The space ($\mathcal{V}$) is associated with the regularity of the solution. Further details on this aspect, particularly when the domain includes an internal boundary or a re-entrant corner, can be found in Babuška and Rosenzweig [28] and Grisvard [29]. It is important to note that the space ($\mathcal{V}$) accommodates discontinuous functions across the crack line. The test function space is similarly defined as:

$$\mathcal{U}_0=\{\mathbf{v}\in\mathcal{V}:\mathbf{v}=0\ \text{ on }\Gamma_u\mathbf{v}\text{ discontinuous on }\Gamma_c\} \tag{33}$$

The weak form of the equilibrium equations can be expressed as follows:

$$\int_\Omega \sigma:\varepsilon(\mathbf{v})d\Omega=\int_\Omega \mathbf{b}\cdot\mathbf{v}d\Omega + \int_{\Gamma_t}\bar{t}\cdot\mathbf{v}d\Gamma \qquad \forall\mathbf{v}\in\mathcal{U}_0 \tag{34}$$

By applying the constitutive equation and the kinematic constraints to the weak form equation, the objective is to determine ($\mathbf{u}\in\mathcal{U}$) that satisfies the equation.

$$\int_\Omega \varepsilon(\mathbf{u}):C:\varepsilon(\mathbf{v})d\Omega=\int_\Omega \mathbf{b}\cdot\mathbf{v}d\Omega + \int_{\Gamma_t}\bar{t}\cdot\mathbf{v}d\Gamma \qquad \forall\mathbf{v}\in\mathcal{U}_0 \tag{35}$$

Belytschko and Black [30] demonstrated that the above formulation is equivalent to the strong form of equation (18), which includes the traction-free conditions on both crack faces. Unlike boundary element methods, this approach allows for straightforward extensions to handle non-linear problems. Fig. 8(a) shows the finite element mesh near a crack tip, where the circled numbers represent the element numbers, and Fig. 8(b) shows the regular mesh without a crack.

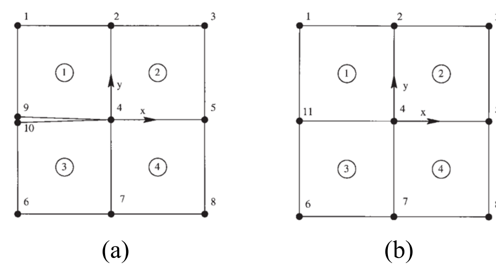

Fig. 8. (a) The finite element mesh near a crack tip, (b) Regular mesh without a crack [25].

5.2. Extended Finite Element Method

The Extended Finite Element Method (XFEM) is a powerful method in advanced engineering for simulating crack formation and propagation in materials without needing precise mesh alignment. Unlike the traditional Finite Element Method (FEM), XFEM can model material discontinuities, such as cracks, by enriching standard finite element techniques with specialized functions. This makes XFEM particularly useful for studying complex material failures across multiple scales. Damage analysis in XFEM focuses on capturing discontinuities and stress distributions around cracks, using enrichment functions and cohesive laws to represent crack surfaces and material behaviorunder stress. The XFEM, introduced by Dolbow in 1999, enhances the finite element approximation through the partition of unity method combined with specialized functions. This approach enables the modeling of discontinuities, such as cracks, using functions like the Heaviside step function, without requiring explicit meshing of the crack itself, as shown in Fig. 9. XFEM, when combined with the partition of unity method, becomes an effective solution for modeling the behaviours of multi-phase materials. Simulation software like ABAQUS provides engineers and researchers with precise control over these methods, enabling in-depth analysis of cracks, material interfaces, and multiple crack interactions in a single model [31].

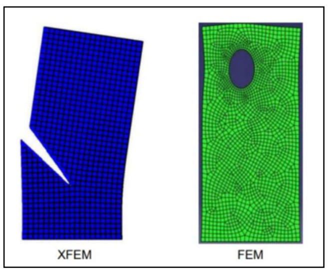

Fig. 9. Difference between FEM and X-FEM [31].

This method is particularly beneficial for complex materials and multi-crack simulations, with step-by-step examples provided for both 2D and 3D crack growth simulations, offering insights into setting up accurate XFEM simulations for various engineering challenges [31]. The Extended Finite Element Method (XFEM) introduces additional degrees of freedom at the nodes of elements intersected by the crack geometry, as illustrated in Fig. 10. by integrating these extra degrees of freedom with specialized shape functions, XFEM significantly enhances the accuracy of crack modeling, enabling precise representation of the discontinuities [32].

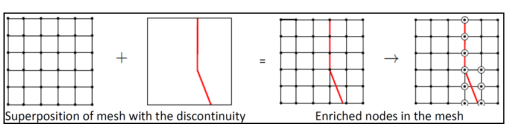

Fig. 10. Definition of the enriched nodes in a mesh of finite elements [32].

Unlike the partition of unity FEM and generalized FEM, which apply enrichments globally across the domain, the Extended Finite Element Method (XFEM) implements enrichments locally, focusing on areas near the crack tip. This localized approach offers a significant computational advantage by reducing the number of enriched nodes. For a point x within an element intersected by a crack, XFEM uses a specialized approximation to calculate displacement at that point.

$$u^{(e)}(x) = u^{FEM} + u^{Enrichement} = \sum_{i=1}^{n} N_i(x)u_i(x) + \sum_{j=1}^{m} \bar{N}_j(x)\psi(x)a_j \quad (36)$$

Here u_i represents the nodal degrees of freedom, a_j denotes the additional degrees of freedom introduced by the enrichment functions $\psi(x)$, applied to nodes within the influence area of the discontinuity. The influence area is defined based on the discontinuity's location. For an edge node, it includes the elements containing the node, while for an interior node (in higher-order elements), it comprises the surrounding element, as shown in Fig. 11.

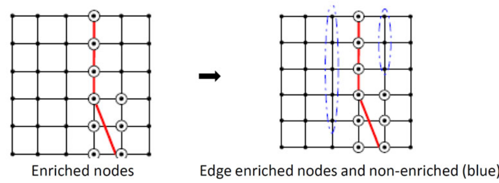

Fig. 11. Nodes enriched by the discontinuity are located along the contour line, either inside or on the edge of the element [32].

The enrichment function $\psi(x)$ in XFEM should be selected based on analytical solutions suited to the type of discontinuity. The primary goal of using different enrichment functions is to accurately model discontinuities and enhance the solution's precision [33]: (i) Accurately replicate the displacement field near the crack tip. (ii) Ensure compatibility of displacements between adjacent finite elements. (iii) Model distinct strain fields on either side of the crack surface. For a standard crack implementation problem, the displacement approximation function at an element node can be expressed as:

$$\begin{aligned} u^{(e)}(x) = u^{FEM} + u^{Enr} = \sum_{i\in 1}^{n} N_i(x)u_i(x) \\ + \sum_{j\in K_D}^{m} \bar{N}_j(x)H(x)a_j + \sum_{j\in K_T}^{m} N_j K(x)b_j \end{aligned} \quad (37)$$

The set (j) includes all nodes, while the set (K) consists of enriched nodes. Among these, K_D represents the enriched nodes associated with the discontinuity, and K_T corresponds to those related to the crack tip. The enrichment functions H(x) and K(x) are utilized for modeling a strong discontinuity, as illustrated in Fig. 12.

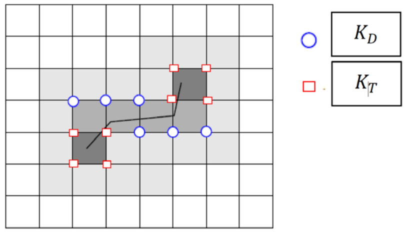

Fig. 12. Definition of the enriched nodes and domains in XFEM [32].

5.3. Fracture Initiation and Propagation

Fracture initiation in ABAQUS begins when the cohesive response of an enriched element starts to degrade, triggered by stresses or strains meeting specified fracture initiation criteria. These criteria are defined through built-in models (summarized in Table 3) or can be customized using the UDMGINI subroutine. A fracture initiates or extends when the fracture criterion (f) reaches a value of 1.0 within a specified tolerance after equilibrium increment.

$$1.0 \le f \le 1.0 + f_{tol} \tag{38}$$

The tolerance f_{tol} can be specified by the user. The default value of f_{tol} is 0.005. if $f > 1.0 + f_{tol}$, the time increment is cut back such that the fracture initiation criterion is satisfied.

Table 3. Damage initiation criterion and their implementation in ABAQUS [34].

Criterion	f	Keywords
Maximum Principal Stress	$f = \frac{\sigma_{\max}}{\sigma^0_{\max}}$	*DAMAGE INITIATION, CRITERION= MAXPS
Maximum Principal Strain	$f = \frac{\varepsilon_{\max}}{\varepsilon^0_{\max}}$	*DAMAGE INITIATION, CRITERION= MAXPS
Maximum Normal Stress	$f = \max\left\{\frac{\langle t_n\rangle}{t_n^0}, \frac{t_s}{t_s^0}, \frac{t_t}{t_t^0}\right\}$	*DAMAGE INITIATION, CRITERION= MAXS
Maximum Normal Strain	$f = \max\left\{\frac{\langle \varepsilon_n\rangle}{\varepsilon_n^0}, \frac{\varepsilon_s}{\varepsilon_s^0}, \frac{\varepsilon_t}{\varepsilon_t^0}\right\}$	*DAMAGE INITIATION, CRITERION= MAXE
Quadratic Normal Stress	$f = \left\{\frac{\langle t_n\rangle}{t_n^0}\right\}^2 + \left\{\frac{t_s}{t_s^0}\right\}^2 + \left\{\frac{t_t}{t_t^0}\right\}^2$	*DAMAGE INITIATION, CRITERION= QUADS
Quadratic Normal Strain	$f = \left\{\frac{\langle \varepsilon_n\rangle}{\varepsilon_n^0}\right\}^2 + \left\{\frac{\varepsilon_s}{\varepsilon_s^0}\right\}^2 + \left\{\frac{\varepsilon_t}{\varepsilon_t^0}\right\}^2$	*DAMAGE INITIATION, CRITERION= QUADE

The symbol $\langle\ \rangle$ known as the Macaulay bracket, indicates that compressive stress alone does not initiate damage. Fracture growth begins only when the stress reaches a critical value: $\langle \sigma_{\max}\rangle = 0$ if $\sigma_{\max} < 0$ and $\langle \sigma_{\max}\rangle = \sigma_{\max}$ if $\sigma_{\max} \ge 0$
Fracture initiation is determined by one of six predefined stress- or strain-based criteria (as summarized in Table 3.) or a user-defined criterion. Once initiated in an enriched region, fracture propagation follows the XFEM-based LEFM criterion [34].

6. Numerical Modeling Workflows

6.1. Initialization of The Numerical modeling

The first step involves the numerical modeling initialization to determine the fracture toughness K_{Ic} to ensure the modiling correctness and accuracy. Numerical modeling of the fracture toughness determination test requires the definition of two independent models with the same geometry. The first is an XFEM model to determine the critical load at which fracture propagation begins, while the second is a stationary fracture model for calculating the stress intensity factors. The test was modeled using plane strain analyses, with identical geometry and material parameters in both models, as presented in Table 4.

Table 4. Input parameters for model verification [2].

Parameter	
$\boldsymbol{E}$(kPa)	1.427×10^7
$\boldsymbol{\upsilon}$	0.2
$\boldsymbol{\sigma}$(kPa)	5560
$\boldsymbol{\phi}$	0.265
$\mathbf{2}\boldsymbol{b}(\boldsymbol{m})$	0.04
$\mathbf{2L}(\boldsymbol{m})$	0.004

The boundary conditions are designed to maintain the verticality of the sample during the loading process, with the top of the sample constrained accordingly, as shown in Fig. 13.

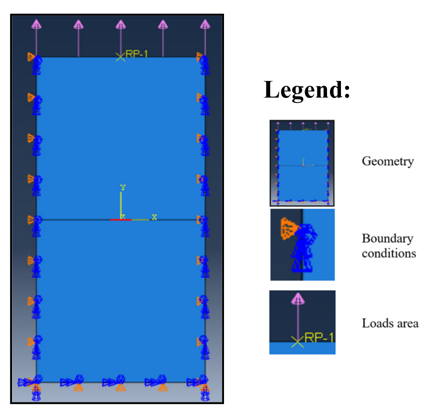

Fig. 13. Geometry, boundary conditions, and loads area for the fracture toughness test.

A conservative approach was taken by fully fixed the bottom of the sample, while the reaction forces at the bottom of the sample redirect the applied load, as shown in Fig. 13. A line load was applied at the midpoint of one end of the plate, with a value of 400 KN/m/min, increasing linearly over each time step. After determining the critical load, it is applied to a stationary fracture model to calculate the stress intensity factor. Accurate results require a mesh with specific characteristics, particularly quadrilateral elements near the crack tip collapsing into triangular shapes to capture the singularity effectively, as shown in Fig. 14.

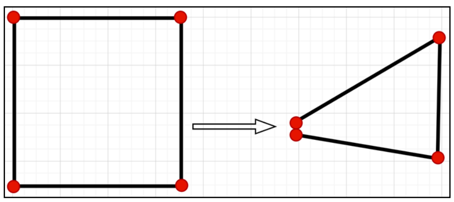

Fig. 14. Linear quadrilateral element degeneration [20].

The degeneration of elements and the collapse of nodes around the crack tip result in a more complex mesh geometry, as illustrated in Fig. 15. And the CPE4; a 4-node bilinear plane strain quadrilateral is used in this modeling. The effects of mesh type and size on the simulation results have been thoroughly discussed in the result and discussion section.

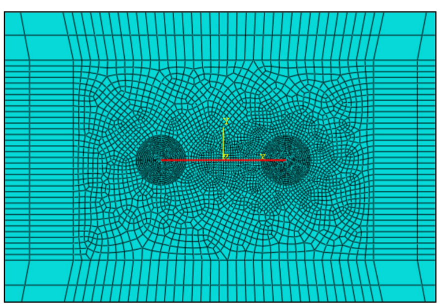

Fig. 15. Denoting the mesh around the crack.

For the stationary fracture model, the mesh is predominantly structured, except near the fracture, where a sweep mesh configuration is used to accommodate the circular geometry, as shown in Fig. 16 (a, b). The model consists of 9002 plane strain linear quadrilateral elements and 9180 nodes.

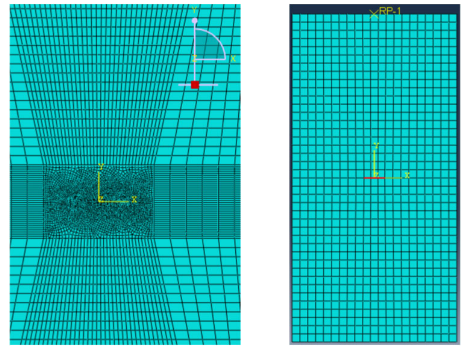

(a) (b)

Fig. 16. (a) Stationary Mesh, (b) XFEM Mesh.

6.2. Numerical Modeling Verification

The second step involves verifying the model through systematic comparison of simulation results. This ensures that the model accurately captures the physical phenomena associated with fracture mechanics, including crack initiation and propagation under specified conditions. Key performance metrics such as stress intensity factors and fracture patterns are used as benchmarks for verification. Verification ensures that the numerical model accurately represents the underlying physical and mathematical formulations. Unlike validation, which compares results with experimental data, verification focuses on assessing numerical correctness through comparisons with analytical solutions, numerical benchmarks, or experimental observations. Additionally, comparing numerical results with Linear Elastic Fracture Mechanics (LEFM) solutions verifies crack propagation accuracy [35]. When analytical solutions are unavailable, verification relies on comparisons with well-established numerical methods such as BEM, DEM, and refined FEM simulations. A mesh convergence study ensures numerical consistency, while experimental comparisons such as breakdown pressure, fracture growth rate, and geometry help validate the model's realism. Sensitivity analyses on material properties, fluid viscosity, and in-situ stresses further refine numerical predictions [36].

To demonstrate the measurement of fracture toughness and the effect of a crack on material behaviour, we consider a bar of unit thickness featuring a central crack of length (2*L*) as shown in Fig. 4. One of the tests for the determination of the fracture toughness is a test on an infinite plate with a center crack that is subjected to tension, as shown schematically in Fig. 4 [19]. Despite its simplicity, the test is challenging to perform in practice. Modeling this test is of significant interest because well-established analytical solutions exist for this loading condition, enabling comparison with the numerical results (Paris C. and Sih G., 1964) [9].

The SIF K_I for an infinite plate with a central crack under tension, assuming LEFM, can be determined using the equation (4). The critical SIF K_{Ic} is determined using equation (5) mentioned in the previous section. The critical fracture energy G_{Ic} calculated using the equation (8) [19]. In the fracture propagation simulation using the XFEM method, the critical load for fracture propagation is determined to be 288 kN (Fig. 17).

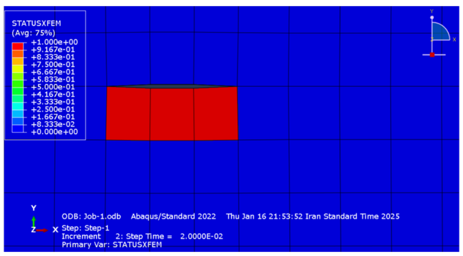

Fig. 17. Status of crack opening using XFEM.

This figure presents the output STATUSXFEM, which indicates the state of fracture propagation. A nonzero value of STATUSXFEM signifies that the fracture has propagated, while a value of one indicates the complete loss of cohesive behaviorin the section [37].

Once the critical load (F_c) is determined, the critical stress intensity factor (K_{Ic}) (also referred to as fracture toughness) can be computed using Equation (5):

$$K_{Ic} = \frac{28800}{2\cdot 0.02}\sqrt{3.14\cdot 0.002}\left(1-\frac{0.002}{2\cdot 0.02}\right)\left(1-\frac{0.002}{2\cdot 0.02}\right)^{-1}$$
$$K_{Ic} = 7200000\cdot 0.0792\cdot 0.95\cdot 1.0266 \quad (39)$$
$$K_{Ic} = 556137.9648\ Pa\sqrt{\text{m}} => 0.556\,\text{MPa}\sqrt{\text{m}}$$

According to Equation (8), the critical fracture energy denoted as (G_{Ic}), can be determined as follows:

$$G_{Ic} = \frac{1-0.2^2}{1.427\cdot 10^{10}}(0.556\cdot 10^6)^2$$
$$G_{Ic} = \frac{0.96}{1.427}30.9136 => 20.796\,\text{N/m} \quad (40)$$
$$G_{Ic} = 0.020\ \text{KN/m}$$

From the output file of the stationary fracture model (Abaqus output data file), the calculated values of the stress intensity factors for different contours can be extracted, as illustrated in Fig. 18. In the stationary fracture model, four contours are recommended for calculating the SIF to ensure computational efficiency and result accuracy [37].

```
                        K  F A C T O R      E S T I M A T E S

CRACK       CRACKFRONT          C O N T O U R S
NAME        NODE SET            1             2             3             4

H-OUTPUT-2_CRACK-1
       -13-          K1:      557.4         558.5         559.5         559.7
                K2:DIRECTION  0.000         0.000         0.000         0.000
        MTS    (DEG):         0.000         0.000         0.000         0.000
                 J from Ks:  4.1054E-03    1.1059E-03    1.1062E-03    2.1072E-03
```

Fig. 18. The K factor estimates contour.

The stress intensity factor is calculated as the average of the values obtained from the specified contours, ensuring that the contour closest to the crack tip is not ignored.

$$K_I = \frac{557.4+558.5+559.5+559.7}{4} \quad (41)$$
$$K_I = 558.775\ \text{KPa} => 0.558\,\text{MPa}\sqrt{\text{m}}$$

To calculate the percentage difference between the theoretical and numerical results, the absolute difference (0.558−0.556) is first determined. This difference is then divided by the theoretical value (0.556) and multiplied by 100. The Python code calculates the percentage difference, which is found to be 0.36%.

7. Result and Discussion

Numerical modeling plays a vital role in understanding fracture mechanics, enabling a detailed analysis of crack behaviorunder various conditions. The presented scenarios investigate critical factors such as crack length, angle, and mesh properties, as well as their effects on displacement, stress intensity, and fracture toughness. These analyses provide valuable insights into the mechanical stability of materials and help validate numerical models against analytical and experimental results.

7.1. Effect of Crack Length on Displacement Curve in (U1) and (U2) Directions

This scenario investigates the effect of crack length on displacement behavior in the (U1) and (U2) directions. The displacement paths (mm) in both directions are illustrated in Fig. 19, where (a) corresponds to (U1) and (b) to (U2). The analysis was performed based on different crack lengths while keeping the crack angle constant. The results highlight how crack length influences the displacement patterns under the applied loading conditions. The associated displacement curves are presented in Fig. 20 for further analysis. The effect of crack length on displacement curves in the (U1) and (U2) directions is significantly influenced by the interaction between crack length, crack angle, and the applied tensile force in the vertical (U2) direction.

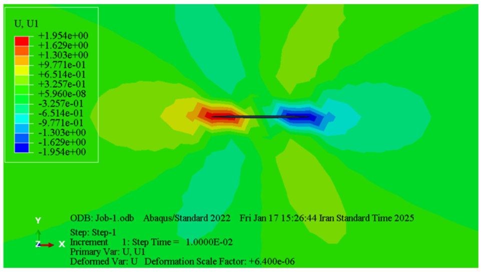

(a)

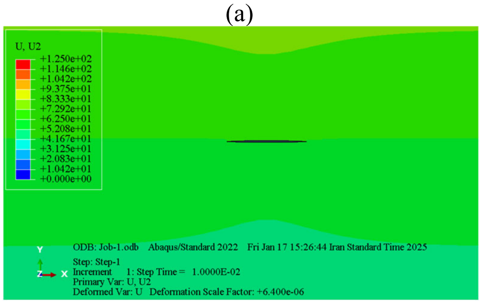

(b)

Fig. 19. Displacement variation (mm) in (a) U1 and (b) U2 direction.

Under initial conditions, with a crack length of 0.004 mm and a specific crack angle, the stress and displacement fields exhibit symmetric behaviour. The displacement in the (U2) is more pronounced due to the dominant tensile load and increases further with intensified stress concentration at the crack tip. When the crack angle changes relative to the X-axis, the orientation and magnitude of displacement curves alter significantly. At certain angles, stress concentrates more in the horizontal direction, leading to increased displacement in the (U1). For other angles, the vertical displacement (U2) remains dominant due to the alignment of the applied tensile force. The displacement curve in the (U1) and (U2) directions are illustrated in the following diagram.

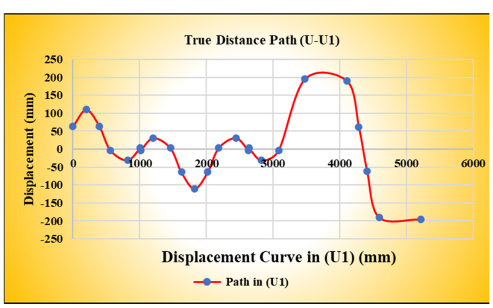

(a)

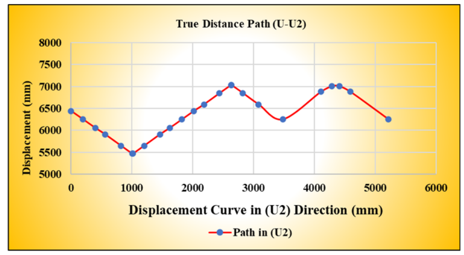

(b)

Fig. 20. Displacement curves (mm): (a) U1 direction; (b) U2 direction.

If the crack length is doubled and the crack angle is set to (45°), the displacement behaviorin both directions; (U1, U2) undergoes significant changes. Doubling the crack length leads to an increased stress intensity near the crack tip, resulting in more pronounced displacements in both directions. The following figures illustrate the changes in crack geometry resulting from doubling the crack length at a 45-degree angle.

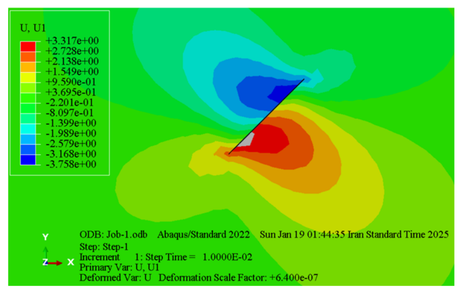

(a)

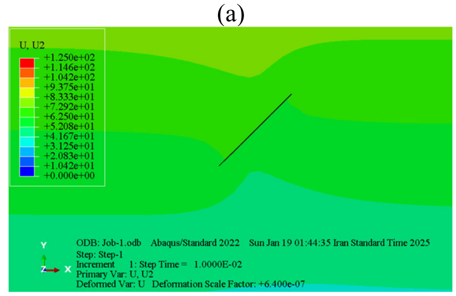

(b)

Fig. 21. Crack Length and Crack Angle Geometry.

As the crack propagates, displacement increases in both the U1 and U2 directions. In the U1 (horizontal) direction, the growth of the crack enlarges the stressed area, which leads to a re distribution of internal forces within the material. This distribution causes a noticeable rise in horizontal displacement, as clearly shown in the U1 displacement diagram. In the U2 (vertical) direction, a similar trend is observed. The applied tensile load in this direction causes vertical displacement to increase, especially near the crack tip where stress distribution is highest. This is illustrated in the U2 displacement diagram, where the vertical displacement grows progressively with crack extension.

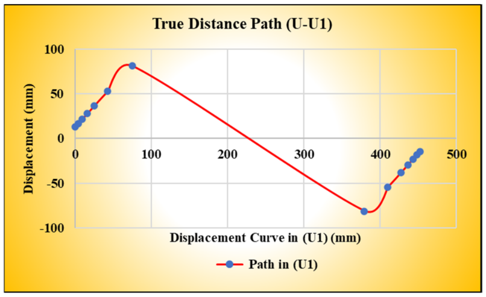

(a)

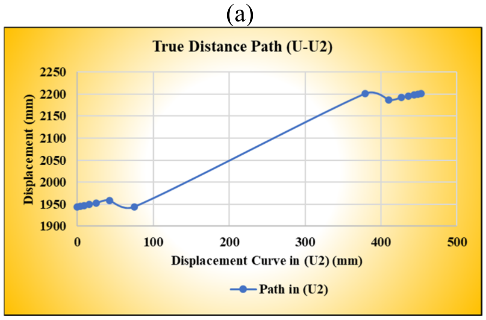

(b)

Fig. 22. Displacement Curves (mm): (a) U1 direction; (b) U2 direction at 45° .

The observed balance between horizontal (U1) and vertical (U2) displacements results from an equal distribution of stress in both directions. Variations in crack geometry play a significant role in influencing crack propagation behaviour, highlighting the critical impact of crack orientation and length on material performance under tensile loading.

7.2. Effect of Crack Angle Modification on Stress Curve in (S11) and (S22) Directions

This scenario examines how changes in crack angle affect the stress distribution in the (S11) and (S22) directions. Fig. 23; (a) and (b) show the initial stress distribution in (S11) and (S22) directions when the crack opens.

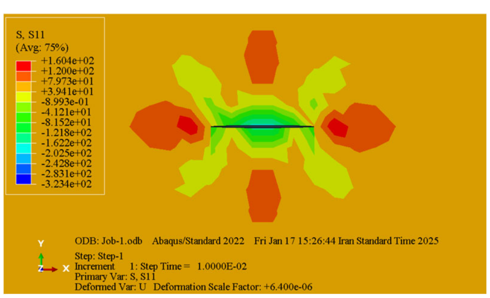

(a)

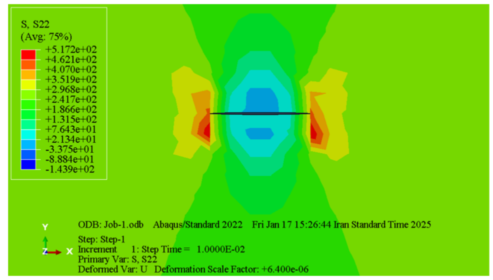

(b)

Fig. 23. Initial stress distribution in: (a) S11 direction; (b) S22 direction.

The stress distribution in the (S11) direction, as shown in the Fig. 24 (a), highlights significant stress concentration at the crack tips, with peak values exceeding (160 MPa). Away from the crack tips, the stress decreases symmetrically, indicating balanced stress propagation along the horizontal axis due to the initial crack orientation of (0°). This symmetric behaviorsuggests uniform stress redistribution in the horizontal direction for the given crack length and orientation. In contrast, the (S22) stress distribution exhibits greater variability, with alternating tensile and compressive stresses reaching values above (400MPa) ((Fig. 24 (b)). The curve is asymmetrical, reflecting the complex vertical stress redistribution near the crack. This emphasizes the stronger influence of vertical stresses under the initial conditions. The stress distribution in (S11) and (S22) directions is shown in the figures below.

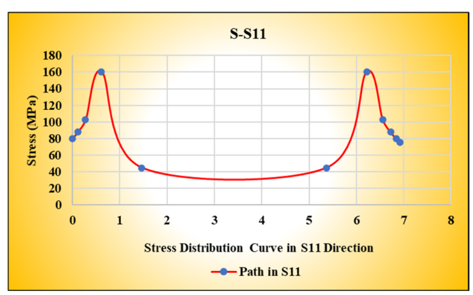

(a)

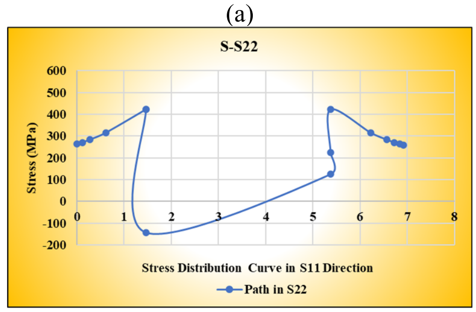

(b)

Fig. 24. Stress distribution curves in (S11) and (S22).

When a tensile force is applied along the y-axis, the stress distribution in the (S11) and (S22) directions is significantly influenced by the crack angle. At 0°, the crack is aligned parallel to the x-axis, while the tensile load acts perpendicular to the crack plane along the y-axis. In this configuration, the (S22) stress component experiences higher concentrations due to the direct alignment of the applied force with the y-axis. The (S11) stress, in contrast, is less critical and relatively evenly distributed.

When the crack angle increases to 45°, the orientation of the crack becomes oblique relative to the applied tensile force. This results in a redistribution of stresses between (S11) and (S22). In the (S11) direction, the oblique crack introduces additional tensile stresses due to the diagonal alignment of the load, causing an increase in stress peaks compared to the 0° crack orientation. On the other hand, in the (S22) direction, the stress distribution becomes more uniform, as part of the tensile force is transferred to the (S11) direction. This redistribution reduces stress concentration near the crack tip in the (S22) path (Fig. 25).

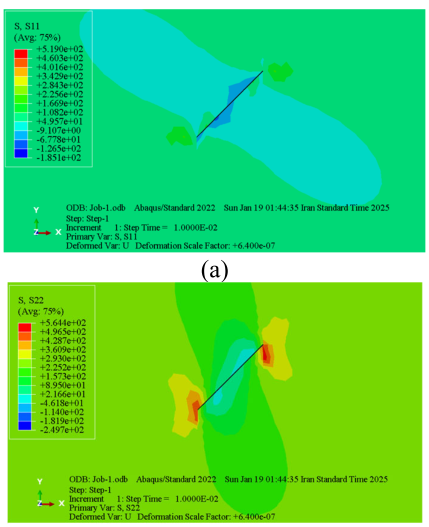

(a)

(b)

Fig. 25. Stress distribution on both sides, accounting for changes in crack angle and length.

Furthermore, the crack angle significantly affects stress distribution under tensile loading along the y-axis. A 45° crack orientation results in stress redistribution, with increased stress in (S11) and reduced distribution in (S22). These variations highlight the critical role of crack geometry in influencing the local stress fields. The stress distribution curves for these changes are illustrated in Fig. 26: (a) (S11); (b) (S22).

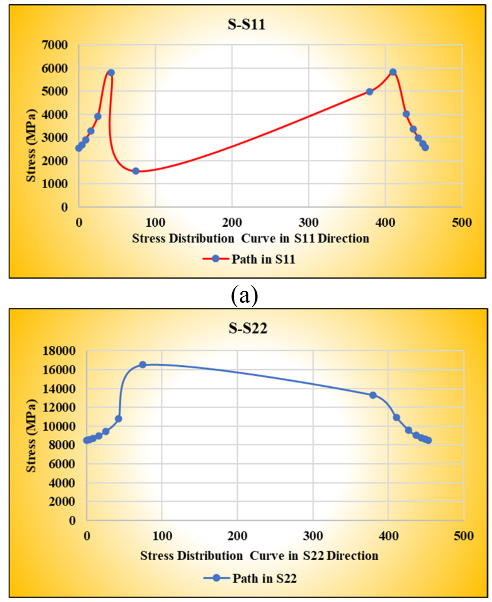

(a)

(b)

Fig. 26. Stress distribution curve on both sides (S11, S22) considering changes in both the crack angle and crack length.

7.3. Effect of Crack Angle Change on Crack Propagation State

This scenario investigates the impact of crack angle variations on crack propagation behaviouring the XFEM. The focus of this investigation is on the change in crack angle and its effect on the crack propagation pattern in different directions. The Fig. 27 (a, b) show the initial crack propagation state and the altered crack angle with the path based on the X-axis direction. As the crack angle increases from 0° to 45°, its propagation behaviorchanges, especially with the application of tensile force along the Y-axis. The tensile force alters the stress distribution around the crack tip, increasing tensile stresses in the Y-direction, which influences the crack's growth direction. As the crack angle shifts, it will tend to propagate toward the direction of higher tensile stress, which is along the Y-axis. This causes the crack path to transition from a horizontal to a diagonal direction.

With the increased crack angle and applied tensile stress, the crack will likely propagate more easily along the Y-axis, shifting from simple horizontal growth to a more complex angled growth. The combined effect of these factors may lead to mixed-mode fracture, where both tensile and shear stresses influence the crack growth, resulting in a more intricate fracture behaviour.

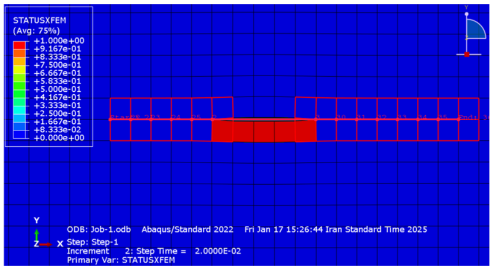

(a)

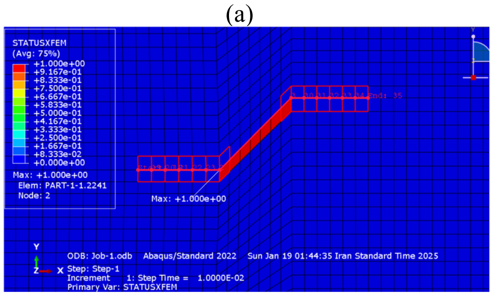

(b)

Fig. 27. Initial crack propagation state (mm) and the path.

The crack growth rate will also be affected by the change in crack angle and the applied tensile force. As the crack angle increases, stress intensity factors change, potentially altering the speed of propagation. While the tensile force may accelerate the crack growth along the Y-axis, the overall growth rate may become more complex as the crack encounters varying material resistances in the new direction. The initial state and altered crack propagation curves under different crack angles and loading conditions are presented in Fig. 28, illustrating the changes in crack growth patterns and propagation paths.

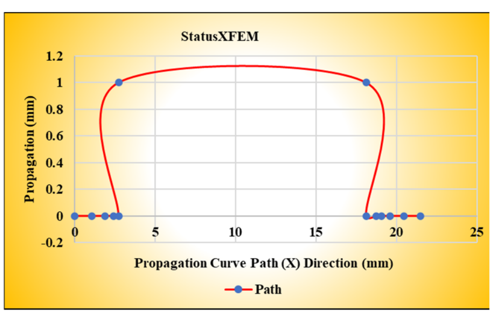

(a)

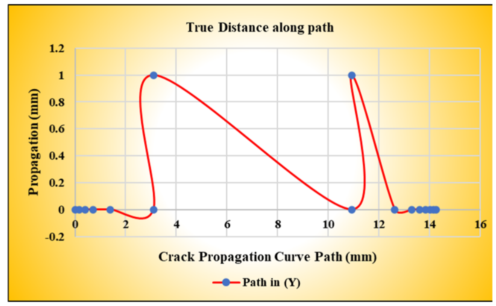

(b)

Fig. 28. Initial state and altered crack propagation curves (mm).

As a result, the application of tensile force along the Y-axis, combined with the variation in crack angle, introduces significant changes in crack propagation behaviour. The crack will deviate from its original horizontal path, potentially leading to a more complex propagation pattern influenced by both tensile and shear stresses. XFEM analysis is essential for accurately modeling these effects and predicting the resulting crack growth behaviour.

7.4. Effects of Mesh Size, Element Type, and Boundary Conditions on Crack Initiation and Propagation

The accuracy and reliability of hydraulic fracture simulations using ABAQUS are significantly influenced by key numerical parameters, including mesh size, element type, and boundary conditions. These factors directly affect the precision of stress distribution calculations, fracture propagation patterns, and overall model stability. A detailed analysis of their effects is presented below.

Effect of Mesh Type and Size: This element type is well-suited for simulating geomechanical problems such as hydraulic fracturing due to its stability and ability to represent stress distributions accurately in 2D domains. The mesh was refined around the anticipated fracture path to capture stress concentrations and crack tip behaviour, while a coarser mesh was applied further from the fracture region to optimize computational efficiency. Mesh refinement is essential for capturing stress intensity at the crack tip and predicting fracture propagation accurately. A finer mesh improves accuracy by better resolving stress gradients near the crack. However, overly small elements can increase computational cost and instability. Mesh size selection is typically determined through a convergence study, where further refinement produces minimal changes in results. In XFEM modeling of hydraulic fracturing, small elements near the crack tip are necessary for precise fracture opening and propagation. Coarse meshes may lead to inaccurate crack paths, unrealistic stress distributions, and underestimating fracture width.

Effect of Boundary Conditions: Boundary conditions significantly influence the stress state in the rock matrix and, consequently, the initiation and propagation of hydraulic fractures. Proper definition of boundary conditions ensures realistic simulation of in-situ stress conditions. For instance, incorrect boundary constraints may lead to artificial stress concentrations or unrealistic deformation modes. In hydraulic fracturing simulations, the following boundary conditions are typically considered:

(i) Far-field stress conditions: These are applied to simulate in-situ stress states and should be consistent with field data. Uneven or incorrect stress application can lead to non-physical fracture propagation patterns. (ii) Injection pressure conditions: The pressure applied at the fracture faces must match the expected injection scheme to accurately replicate fluid-driven fracture growth. Sudden pressure changes or improper loading rates can lead to numerical instabilities. (iii) Symmetry conditions: In cases where symmetry is used to reduce computational cost, appropriate symmetry constraints must be applied to avoid unintended stress artifacts.

In the present XFEM-based numerical framework, fracture-related parameters, including damage initiation criteria, damage evolution parameters, and fracture energy, were incorporated into the formulation to accurately simulate crack initiation and propagation. These parameters control the onset of fracture, progressive damage evolution, and energy dissipation during crack growth, and therefore have a direct influence on the predicted fracture behavior. In the present study, these parameters were appropriately defined and included in the numerical model. However, the sensitivity analysis was focused on crack geometry, material properties, mesh characteristics, element type, and boundary conditions, as these parameters were directly associated with the objectives of this research and their effects on stress distribution, displacement response, and crack propagation behavior were systematically investigated.

7.5. Sensitivity Analysis

To assess the sensitivity of the model to variations in material properties, a parametric study was conducted by systematically altering the elastic modulus, load values, and Poisson's ratio from the given values in Table 4. For the sensitivity analysis of the model, the parameter values are systematically varied relative to the baseline values provided in Table 5. Each parameter is tested once with a reduced value and once with an increased value compared to the initial values. Analysis revealed the following trends:

Table 5. Input parameters for sensitivity analysis.

Parameters	reduced Value	increased Value
$\boldsymbol{E}$(kPa)	1.627×10^7	1.227×10^7
$\boldsymbol{\upsilon}$	0.25	0.19
$\boldsymbol{\sigma}$(kPa)	6000	4500

Young's modulus represents the stiffness of the material. As the value of E increases, the material becomes stiffer and more deformation resistant. This increased stiffness leads to a reduction in crack opening because more energy is required to deform the rock. Crack propagation also becomes more difficult unless additional stress is applied. Conversely, a decrease in Young's modulus softens the rock, which results in greater crack opening and allows the crack to propagate more easily under lower stress. However, crack growth in softer materials may be more unstable and complex. Poisson's ratio indicates the tendency of a material to expand laterally under longitudinal stress. An increase in ν implies greater lateral expansion, which slightly restricts crack opening. It may also influence the crack path, especially under anisotropic stress conditions. On the other hand, decreasing the Poisson's ratio slightly increases crack opening and typically results in a more stable and straighter crack path, as lateral constraints are reduced (Fig. 29). Applied stress is the main driving force behind rock failure and crack propagation. Increasing the applied stress provides the energy needed for crack growth, significantly enhancing both crack opening and length. Under such conditions, cracks propagate more easily and in favorable orientations. In contrast, decreasing the stress limits the available energy for crack propagation, potentially halting the process. Only cracks with favorable orientation and low resistance may continue to grow in such cases).

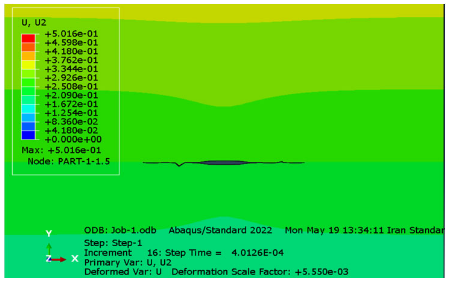

(a)

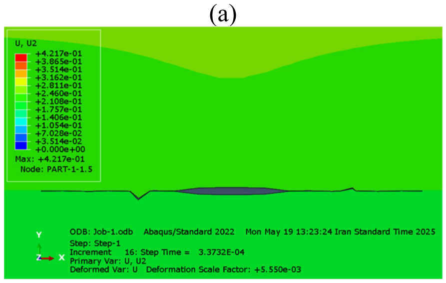

(b)

Fig. 29. Crack Opening Displacement (mm) Based on Sensitivity Analysis of the Model.

Table 6. Impact of Input Parameters Variation on Crack Behaviour.

Parameters	Increase (↑)	Decrease (↓)
(E)	Crack opening ↓, Crack propagation ↓	Crack opening ↑, Crack propagation ↑
(ν)	Crack opening ↓, Higher path deviation↑	Crack opening ↑ (slightly), Straighter path ↑
(σ)	Crack opening ↑, Crack propagation ↑	Crack opening ↓, Higher chance of halted growth ↑

8. Conclusion

This study provides key insights into the role of crack geometry in hydraulic fracturing simulations using XFEM. By focusing on the influence of crack length, angle, and stress distribution, it is evident that these factors play a critical role in fracture propagation, which is crucial for optimizing hydraulic fracturing strategies in unconventional reservoirs:

- Crack Length and Propagation: Longer cracks lead to higher stress intensity and more significant displacement magnitudes. This highlights the importance of controlling crack size during hydraulic fracturing to avoid premature propagation, which could reduce the efficiency of fracture networks.
- Crack Orientation and Stress Redistribution: The crack angle directly affects the stress distribution, with cracks reorienting toward regions of higher tensile stress. This behavioris vital for optimizing fracture directionality and ensuring that fractures propagate toward desired reservoir zones for enhanced productivity.
- Fracture Toughness and Stress Intensity: The relationship between crack length and fracture toughness suggests that longer cracks reduce material resistance to fracture, emphasizing the importance of managing crack propagation to maintain reservoir integrity and prevent excessive fracture growth.
- Mesh Size and Numerical Considerations: The accuracy of fracture simulations is highly dependent on mesh refinement, element type, and boundary conditions. Ensuring proper resolution, particularly near the crack tip, is crucial for predicting fracture paths and stress distributions with high fidelity.
- Increasing E makes the rock stiffer, reducing crack opening and propagation, while decreasing E softens the rock and facilitates crack growth.
- A higher ν slightly restricts crack opening and affects its path, whereas a lower ν increases opening and stabilizes the crack path.
- Higher applied stress provides energy for crack growth, enhancing propagation, while lower stress may limit or halt crack development.

Overall, XFEM proves to be a robust tool for capturing complex fracture behaviors in low-permeability formations and provides valuable insights into the fundamental mechanisms of crack initiation and propagation. The main contribution of this study is the development and application of an XFEM-based numerical framework for systematically evaluating the effects of crack geometry, mechanical properties, and numerical parameters on fracture evolution. The results demonstrate that crack characteristics, material properties, and modeling conditions significantly influence stress distribution, displacement response, and crack propagation behavior, providing a clearer understanding of the mechanisms controlling fracture development. However, the present study is based on a simplified mechanical framework, and further validation against laboratory hydraulic fracturing experiments, published benchmark studies, and field-scale observations is required to further evaluate the applicability of the proposed XFEM approach under realistic hydraulic fracturing conditions. Future research should focus on developing fully coupled hydro-mechanical XFEM models, 3D simulations for more accurate crack propagation modeling, incorporating fluid-related effects such as pressure and viscosity variations during fracturing, and considering material heterogeneity to better predict fracture behavior. Furthermore, coupling XFEM with fluid flow models could provide a more integrated approach by capturing the interaction between crack growth and injection fluid, thereby improving fracture design optimization and applicability in unconventional reservoirs.

9. References

[1] Veatch, R. W., Jr., & Moschovidis, Z. A. (1986). *An overview of recent advances in hydraulic fracturing technology*. Society of Petroleum Engineers (SPE 14085). DOI: 10.2118/14085-MS.

[2] Medinas, M. T. L. F., Pereira, M. J. C., et al. (2015). *An extended finite element method (XFEM) approach to hydraulic fractures*.

[3] Ademola, O. R. (2020). *Unconventional reservoir*. Seminar submitted to the Department of Geophysics, University of Ilorin, Ilorin, Nigeria, in partial fulfillment of the requirements for the award of the Bachelor of Science (B.Sc. Hons.) degree in Geophysics.

[4] Lake, L. W. (Ed.). (2007). *Petroleum Engineering Handbook: Production Operations Engineering* (Vol. 4). Society of Petroleum Engineers.

[5] Montgomery, C. T., et al. (2010). *Hydraulic fracturing: An enduring technology*. Retrieved from http://store.spe.org/Legendsof-Hydraulic-

[6] Chen, Z. (2013). An ABAQUS implementation of the XFEM for hydraulic fracture problems. In *ISRM International Conference for Effective and Sustainable Hydraulic Fracturing 2013* (pp. 725–739). DOI: 10.5772/56287.

[7] Moradi, A., Tokhmchi, B., & Fatehi Marji, M. (2016). Indirect boundary element analysis of hydraulic fracturing and natural fractures in hydrocarbon reservoirs. *Research on Analytical and Numerical Methods in Mining Engineering*, 11. (in Persian).

[8] Abdollahipour, A., Fatehi Marji, M., Yarahmadi Bafghi, A., & Gholamnejad, J. (2016). Numerical investigation of effect of crack geometrical parameters on hydraulic fracturing process of hydrocarbon reservoirs. *Journal of Mining & Environment, 7*(2), 205–214. DOI: 10.22044/jme.2016.532.

[9] Cruz, F., Roehl, D., & Vargas, E. do A. (2019). An XFEM implementation in Abaqus to model intersections between fractures in porous rocks. *Computers and Geotechnics, 112*, 135–146. DOI: 10.1016/j.compgeo.2019.04.014.

[10] Dontsov, E. V., & Suarez-Rivera, R. (2020). Propagation of multiple hydraulic fractures in different regimes. *International Journal of Rock Mechanics and Mining Sciences, 128*. DOI: 10.1016/j.ijrmms.2020.104270.

[11] Azarov, A., Patutin, A., & Serdyukov, S. (2021). Hydraulic fracture propagation near the cavity in a poroelastic media. *Applied Sciences, 11*(22). DOI: 10.3390/app112211004.

[12] Haidari, M., Fatehi Marji, M., & Merzaian, Y. (2022). Investigation of the effect of in situ and porosity stresses on crack growth mechanism in hydraulic fracturing by the displacement discontinuity numerical method. *Journal of Petroleum Geomechanics*. DOI: 10.22034/anm.2024.21058.1620. (in Persian).

[13] Zeerak, M. R., Fatehi Marji, M., & Sanei, M. (2023, March). Investigating hydraulic fracture models for production enhancement of unconventional hydrocarbon reservoirs. In *Proceedings of the 4th National Petroleum Geomechanics Conference*. Retrieved from https://civilica.com/doc/1618288/

[14] Fatehi Marji, M., Lak, M., & Sanei, M. (2023). The explosive fracturing technique analysis for highly low permeable reservoirs using analytical, displacement discontinuity, and finite difference coupled method. *Journal of Petroleum Geotechnics*. DOI: 10.22107/JPG.2023.412506.1208.

[15] Esfandiari, M., & Pak, A. (2023). XFEM modeling of the effect of in-situ stresses on hydraulic fracture characteristics and comparison with KGD and PKN models. *Journal of Petroleum Exploration and Production Technology, 13*(1), 185–201. DOI: 10.1007/s13202-022-01545-7.

[16] Zeerak, M. R., Fatehi Marji, M., Sanei, M., Najafi, M., & Abdollahipour, A. (2025). Numerical modeling of hydraulic fracturing for crack growth mechanism investigation in rocks using XFEM with a BEM-based verification. *Journal of Mining and Environment*. DOI: 10.22044/jme.2025.15836.3047.

[17] Yazdani, M., Fatehi Marji, M., Najafi, M., & Sanei, M. (2025). Simulating the hydraulic fracturing mechanism around hydrocarbon wellbores with emphasis on its effects on sand production. *Journal of Mining and Environment, 16*(1), 241–258. DOI: 10.22044/jme.2024.14049.2619.

[18] Feng, X., Fatehi Marji, M., & Abdollahipour, A. (2017). *Rock mechanics and engineering*. Springer.

[19] Economides, M. J., & Nolte, K. G. (2000). *Reservoir stimulation* (3rd ed.). John Wiley & Sons.

[20] Dassault Systèmes. (n.d.). *Modeling fracture and failure with Abaqus*.

[21] Dassault Systèmes. (2020). *Modeling fracture and failure with Abaqus*.

[22] Huang, R. Q., Wu, L. Z., & Li, B. (2019). Crack initiation criteria and fracture simulation for precracked sandstones. *Advances in Materials Science and Engineering, 2019*. DOI: 10.1155/2019/9359410.

[23] Bui, Q. V. (2011). A modified Benzeggagh–Kenane fracture criterion for mixed-mode delamination. *Journal of Composite Materials, 45*(4), 389–413. DOI: 10.1177/0021998310376105.

[24] Kenane, M., & Benzeggagh, M. L. (1997). Mixed-mode delamination fracture toughness of unidirectional glass/epoxy composites under fatigue loading. *Composites Science and Technology, 57*, 597–605. DOI: 10.1016/S0266-3538(97)00021-3.

[25] Moës, N., Dolbow, J., Belytschko, T., & Moës, N. M. (1999). A finite element method for crack growth without remeshing. *International Journal for Numerical Methods in Engineering, 46*(1), 131–150. DOI: 10.1002/(SICI)1097-0207(19990910)46:13<131::AID-NME726>3.0.CO;2-J.

[26] Chen, Z. (2013, June 16–21). *Implementation of the XFEM for hydraulic fracture problems*. In *Proceedings of the 13th International Conference on Fracture (ICF13)*, Beijing, China.

[27] Heydari, M., Reza, M., Emamqeysi, A., & Sanei, M. (2022). Finite element analysis of wellbore stability and optimum drilling direction and applying NYZA method for a safe mud weight window. *Analytical and Numerical Methods in Mining Engineering, 11*(29), 67–76. DOI: 10.29252/ANM.2022.16945.1511.

[28] Babuška, I., & Rosenzweig, M. B. (1972). A finite element scheme for domains with corners. *Numerische Mathematik, 20*(1), 1–21. DOI: 10.1007/BF01436639.

[29] Grisvard, P. (2011). *Elliptic problems in nonsmooth domains*. Society for Industrial and Applied Mathematics (SIAM). DOI: 10.1137/1.9781611972030.

[30] Belytschko, T., & Black, T. (1999). Elastic crack growth in finite elements with minimal remeshing. *International Journal for Numerical Methods in Engineering, 45*, 601–620.

[31] Experts of CAE Assistant Group. (n.d.). *Extended finite element method in Abaqus (XFEM tutorial)*.

[32] Duarte, A., & Simone, A. (n.d.). *An introduction to partition of unity and generalized finite element methods*.

[33] Mohammadi, S. (2008). *Extended finite element method for fracture analysis of structures*. Blackwell Publishing.

[34] Sepehri, J., Soliman, M. Y., Morse, S. M., Menouar, H., House, W., & Sheridan, M. (2014). Application of extended finite element method (XFEM) to simulate hydraulic fracture propagation from oriented perforations. *Society of Petroleum Engineers*. DOI: 10.2118/SPE-173342-MS.

[35] Lecampion, B., Bunger, A., & Zhang, X. (2018). Numerical methods for hydraulic fracture propagation: A review of recent trends. *Journal of Natural Gas Science and Engineering, 49*, 66–83. DOI: 10.1016/J.JNGSE.2017.10.012.

[36] Budyn, É., Zi, G., Moës, N., & Belytschko, T. (2004). A method for multiple crack growth in brittle materials without remeshing. *International Journal for Numerical Methods in Engineering, 61*(10), 1741–1770. DOI: 10.1002/NME.1130.

[37] Abass, H. H., Meadows, D. L., Brumley, J. L., Hedayati, S., & Venditto, J. J. (1995). Oriented perforations: A rock mechanics view. In *Proceedings of the Middle East Oil Show* (Vol. 1, pp. 13–27). Society of Petroleum Engineers. DOI: 10.2118/28555-MS.